JOURNAL OF Applied Polymer SCIENCE

Thermal Conductivity of Anisotropic, Inhomogeneous High-Density Foam Calculated from Three-Dimensional Reconstruction of Microtome Images

Jan Peder Hegdal,[1] Terje Rosquist Tofteberg,[2] Trond Schjelderup,[3] Einar Louis Hinrichsen,[2] Frode Grytten,[2] Andreas Echtermeyer[1]

[1]Department of Engineering Design and Materials, Norwegian University of Science and Technology, Trondheim 7034, Norway
[2]SINTEF Materials and Chemistry, Oslo 0373, Norway
[3]Bredero Shaw, Orkanger 7300, Norway
Correspondence to: J. P. Hegdal (E-mail: jphegdal@brederoshaw.com)

ABSTRACT: An effective method is developed to predict the thermal conductivity of thick foam insulation on offshore oil and gas pipelines. High-resolution three-dimensional (3D) images (212 megavoxels) spanning macroscopic sample volumes ($38 \times 19 \times 4$ mm^3) are obtained and used to create a 3D geometry of the foam. A gravimetric technique is developed to measure the mass density through the foam thickness and used to verify the 3D geometry. The local anisotropic thermal conductivity through the thickness of the foam is calculated using the finite element method on the 3D geometry and the results are verified against measurements and found to be in good agreement. Results show that thermal conductivity is dependent on morphology. For the highly anisotropic part of the foam where the long axes of the bubbles are oriented parallel to the axial direction of the pipe, the radial thermal conductivity is lowered significantly compared to more isotropic foam. © 2013 Wiley Periodicals, Inc. J. Appl. Polym. Sci. 130: 1020–1028, 2013

KEYWORDS: oil & gas; thermal properties; foams; morphology; properties and characterization

Received 29 November 2012; accepted 27 February 2013; published online 17 April 2013
DOI: 10.1002/app.39238

INTRODUCTION

Subsea oil and gas pipelines transport fluids over long distances on the seabed. The temperature of the oil upon leaving the well head is in the region of 50–200°C, whereas the surrounding water typically is 4–10°C. It is important to keep the oil warm and the viscosity low to ease transport of the oil through the pipe. Even more critical, in the case of halts in oil production the oil may cool down so much that hydrates starts precipitating, clogging the line. Plugs of hydrates and wax are difficult, sometimes impossible to remove.[1–4]

To keep the oil inside the pipeline warm, insulation is very often applied on the outside. Figure 1 shows a section of typical polymer insulation removed from the pipe. The insulation should have low thermal conductivity and it has to withstand the high hydrostatic pressure from the water. Thick layers of high-density polymeric foams with small air bubbles are typically used for this application as they can withstand the pressure and have low thermal conductivity.[5–9]

The surface of the pipe is precoated to ensure good bonding and the insulation is applied by an extruder. A blowing agent is mixed into the polymer and fed into the extruder. The blowing agent decomposes to produce gas and expands upon leaving the extruder creating bubbles and the foam structure as a result. Ideally, the bubbles should be spherical and evenly distributed throughout the radial thickness. But the process deforms the bubbles through shear, causing slightly elliptical bubbles. Further, the distribution of the bubbles through the thickness is not even.

The extrusion process parameters must be optimized to get the highest compressive stiffness and lowest thermal conductivity. Such optimization is possible only if the morphology of the produced foam structure can be well characterized/measured and the thermal conductivity can be predicted from these measurements. This article will describe how the bubble morphology can be measured and how thermal conductivity can be predicted from the measurements using a numerical simulation.

Today, thermal conductivity is calculated analytically based on the mass density of the foam, ignoring the detailed morphology. However, the anisotropy is expected to have significant influence on thermal conductivity.[10,11] Analytical expressions for

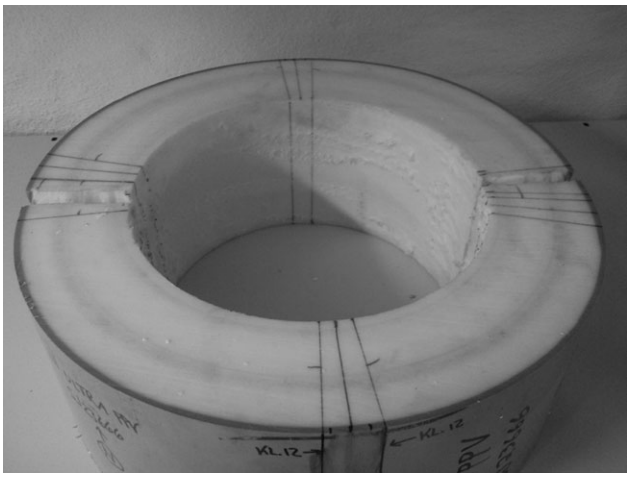

Figure 1. A section of polymer pipe insulation removed from the pipe. Total thickness of the insulation is 80 mm of which two layers with a total thickness of 64 mm are high-density foam.

both elastic and conductive properties of the composite material also exist if a heterogeneous material can be approximated by identical spheroid inclusions of one material within another.[12,13] When the inclusions have very different shapes, the predictions are not accurate anymore.[14] Numerical predictions of thermal conductivity from a two-dimensional (2D) model for low-density PE foam and a three-dimensional (3D) geometry for low-density PU foam also exist.[15,16] But a 2D model cannot properly account for the bubble anisotropy and low-density foam behaves very differently from the high-density foams investigated here, showing the need for a better model, as presented in this article.

For polymers, a commonly used method for probing 3D microstructure is X-ray-computed microtomography which gives resolutions down to a few micrometer and is nondestructive.[17] For voxel dimensions down to tens of a nanometer, focused ion beam tomography can be used.[18] However, for the pipes investigated in this study the size of the samples (outer pipe diameter, 433 mm) was prohibitive for these high-resolution, nondestructive methods. The high resolution is also not needed to characterize bubbles in the millimeter size range. Scanning of microtome slices was chosen to determine the morphology.

The morphology of the real foam was characterized by an advanced 3D image analysis based on overlaying 2D images. This approach has a long history. In 1918, Forsman[19] projected images of pearlite cross-sections onto cardboard. By choosing cardboard of appropriate thickness and cutting away the alpha-ferrite phase, he was able to produce 3D models of the cementite lamellae. In the last two decades, automated sectioning, digital image acquisition, automated section alignment, and image segmentation have made possible the automated construction of a 3D material structure by serial sectioning.[20]

Tofteberg et al. performed image segmentation on high-impact-modified polystyrene (HIPS) foam taken from a production scale subsea pipe. In total, 132 consecutive microtome slices were taken from the innermost foam layer of the insulation as shown in Figure 1. Individual foam bubbles were identified, thereby quantifying average bubble number density, bubble orientation, bubble size, and bubble aspect ratio as a function of radial (thickness) position in the layer.[21] Some difficulties arise in the image segmentation owing to thresholding, the finite thickness of the microtomy slices, correctly separating foam cells, and aligning sequences of microtomy images. The latter two problems were successfully dealt with by sophisticated algorithms. The first and second problems leave a systematic error in the bubble size; hence, derived morphological properties such as the mass density will have a systematic error. In this article, the characterization of the foam morphology also includes spatial variations in the plane in addition to the thickness information. This is described in a complete 3D geometry extracted from the abovementioned slices. The 3D geometry is validated by calibrating it to gravimetric measurements through the thickness of the foam layer.

The well-characterized 3D geometry is then used to predict thermal conductivity. This article investigates a commercially made high-density, anisotropic, inhomogeneous HIPS foam and will describe how the complete 3D geometry is applied to predict the thermal conductivity by the finite element method, and the predictions are compared to experiments.

GRAVIMETRIC MEASUREMENTS

Gravimetric measurements were taken through the thickness of the foam layer to measure the local mass density. The result was used to calibrate the 3D geometry of the foam layer.

Specimen Preparation

A sample was taken from the multilayer polystyrene insulation system as shown in Figures 1 and 2. The sample was taken from the same layer and as close as possible to the sample

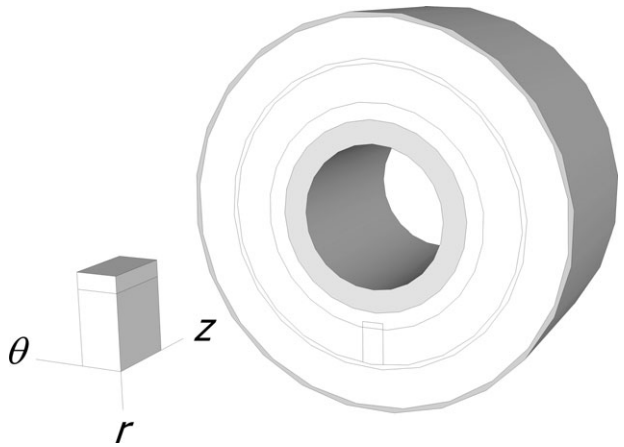

Figure 2. Sketch of the pipe insulation system. Layers of HIPS (black and white) have been applied onto a steel pipe (gray). The two thick layers (light gray) are foamed HIPS. The specimen was taken from the innermost foam layer in the indicated position. The outer foam layer has the same characteristics as the inner foam layer and was not studied here. The *r*-, *θ*-, and *z*-directions in the cylindrical coordinate system of the pipe are used to define directions in the specimen. The coordinates shown are local specimen coordinates and named with cylindrical names to illustrate the orientation of the specimen in the pipe.

Applied Polymer SCIENCE

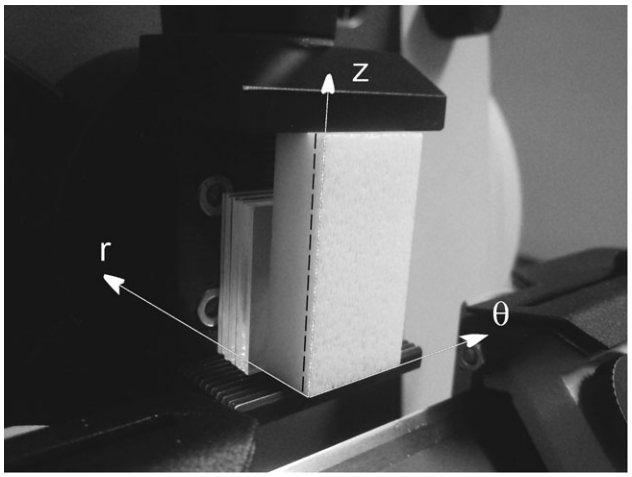

Figure 3. The cuboid fixed in the microtome grips. The microtome moves the specimen vertically up and down, advancing it onto the knife in the downward movement and retracting it when moving up.

investigated by Tofteberg et al. The investigated layer was 36.6 mm thick and made from chemically foamed HIPS. The sample was prepared into a cuboid shape specimen with a base $w = 19.5$ mm wide in the pipe's hoop direction, $l = 37.3$ mm long in the axial direction, and $h = 42.9$ mm high in the radial direction. The measurements were performed with a 0.01-mm resolution caliper and the respective measurements varied within ± 0.1 mm. The average density of the cuboid was 834 ± 6 kg/m^3. Part of the inner polystyrene layer was included in the specimen for gripping. Figure 2 shows how the specimen coordinate system is defined.

Microtomy

A Leica Supercut 2065 rotary microtome fitted with a fixed D-profile steel knife and nonorienting (standard) specimen holder was used to cut thin slices of the specimen (Figure 3). The microtome moved the specimen vertically up and down, advancing it onto the knife in the down stroke and retracting it slightly away from the blade when moving back up. The specimen was positioned in the holder so that the blade was cutting in the positive z-direction and advancing the specimen in the negative r-direction. Each cut produced a $t = 150$ μm thick slice of the specimen, which was the maximum cutting thickness for the microtome. The cutting speed was fixed at 23 mm/s.

Morphological Parameters

Image analysis was performed on the slices to establish the most relevant morphological parameters of the foam. Each foam bubble was fitted with an ellipse, and the centroid, orientation and magnitude of the minor and major axis was measured as a function of radial position in the foam. The foam morphology is roughly homogenous in the z- and θ-direction, and hence each bubble was approximated by an ellipsoid with two equal minor half axes. Bubble size was described by calculating an equivalent bubble radius $r_{eq} = 4/\pi a^{1/3} b^{2/3}$, where a and b are the apparent ellipse major and minor half axis, respectively. The area number density is computed from the number of bubbles in the micrograph. Bubble orientation is described by the angle θ between the major axis and the extrusion direction. The bubble aspect ratio is the ratio between major and minor axis lengths.

Gravimetric Measurements

To measure the inhomogeneous density of the polymer foam, microtome slices were weighed on a Mettler Toledo A204 Delta Range with a resolution of 0.1 mg. To reach a compromise between good spatial resolution and density uncertainty, groups of n microtome slices were weighed together. The density in one such group is

$$\tilde{\rho}(r) = \frac{m}{lwnt\rho_0} \tag{1}$$

where m is the measured mass, l and w are the outer dimensions of the cuboid, and t is the thickness of a microtome slice. The density is normalized with the density of the solid polymer $\rho_0 = 1040$ kg/m^3. The radial position r is the mean radial position within the group measured. There was a clearly identifiable interface between the foam layer and the inner layer which was defined as $r = 0$. The first microtome slice started at $r_0 = 2.60$ mm and the radial position r of the other measurements was found by adding the number of microtome slices $r = r_0 + n_r t$.

Uncertainty of Method

The knife exerts a compressive stress on the specimen during the cutting action. The compressive strain, and hence the thickness of the specimen, varies slightly through the length of a cut and in between cuts. For instance, if the previous slice was overcut, that is too thick, the compressive force in the next cut will be lower, and the slice will be thinner. Slices were therefore mostly grouped in sextets to get a relatively smaller thickness variation. It is estimated that the total thickness of six slices was 900 ± 11 μm. Resolution in the spatial dimension was still very good, but in regions with a high-density gradient it was opted to use only three slices in the groups. The thickness of three slices was estimated to be 450 ± 6 μm.

Table I lists the typical values and their uncertainties for the variables used to calculate the density. An approximate expression for the total relative uncertainty in a density measurement was derived from the total derivative of (eq. 1):

$$\frac{\Delta\tilde{\rho}}{\tilde{\rho}} = \left[\left(\frac{\Delta m}{m}\right)^2 + \left(\frac{\Delta l}{l}\right)^2 + \left(\frac{\Delta w}{w}\right)^2 + n\left(\frac{\Delta t}{t}\right)^2\right]^{\frac{1}{2}} \tag{2}$$

From this equation and Table I, it is clear that the thickness measurement dominates the uncertainty in $\tilde{\rho}$. The uncertainty in radial position r can be expressed as

Table I. Value, Uncertainty, and Unit for the Parameters l, w, h, and t

Parameter	Value	Uncertainty
m (g)	≥0.2330	0.0001
l (mm)	37.3	0.1
w (mm)	19.5	0.1
t (μm)	150	4.5

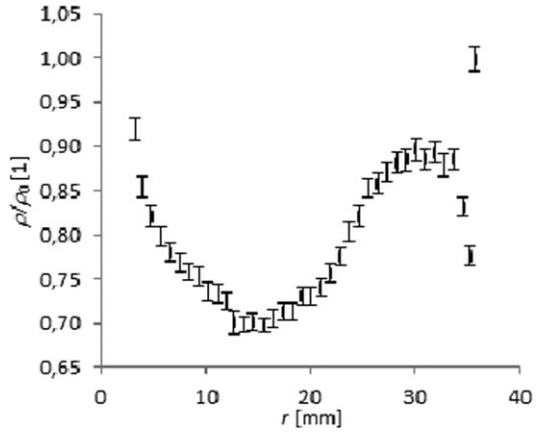

Figure 4. The relative density of the insulation as a function of the radial position.

$$\Delta r = (n_r \Delta t^2)^{\frac{1}{2}} \tag{3}$$

The uncertainty of the measurement of the radial position r increases with the distance from the origin, and this could have been minimized by taking regular measurements of the cuboid height during cutting, thereby removing the additive error and hence the r-dependence. The spatial resolution was, however, deemed sufficient. According to eq. (2), the uncertainty in the density is <1.5% and according to eq. (3) the spatial resolution is <70 μm. Figure 4 shows the relative density through the foam thickness indicated by error bars.

There is a risk of dust being created if the foam structure is particularly fragile, the material is brittle, or the knife is insufficiently sharp. Very little dust was observed in this procedure and whatever could be collected was weighed together with the slices. The mass of dust associated with any one cut was <0.1 mg and thus neglectable.

THERMAL CONDUCTIVITY MEASUREMENTS

Measurements of thermal conductivity were taken at eight positions through the thickness of the foam. The results were used to verify thermal simulations on the 3D geometry.

Heat Flow Meter

A Fox 50 (ASTM C518 and ISO 8301 compliant) comparative heat flow meter instrument from LaserComp (USA) was used for measuring the thermal conductivity of the foamed polystyrene.[22,23] The Fox 50 operates by clamping a specimen disk (with plane and parallel surfaces) between two temperature-controlled plates. Heating elements and water cooling keep the temperatures of the upper and lower plates at a steady difference so that a gradient is maintained through the specimen. Transverse gradients are kept at a minimum by insulating the edge of the disk. The temperature is measured by temperature sensors placed under a thin layer of thermal paint on each plate. Heat flow is measured by one heat flux transducer embedded in the surface of each plate. The signal outputs over the upper and lower transducers are indirect measurements of the heat flow rate through the specimen, which together with the specimen thickness, surface resistance, and differential temperature are used to calculate the thermal conductivity. A calibration in the relevant temperature range on standards with known, similar thermal conductivity must be used to convert the transducer output value to a heat flow rate value.

Heat Equation

Steady-state heat transport in an isotropic, homogenous solid material is described by Fourier's law

$$\vec{j} = -k\vec{\nabla}T, \tag{4}$$

where $\vec{j}$ is the heat flux, T is the temperature, and k is the isotropic thermal conductivity of the material. Thermal conductivity will typically increase with temperature, and hence $k = k(T)$. Here, the specimen is of finite thickness and T would be the average temperature in the middle of the specimen. Hence, it is important to note that the specimen is made of a sufficiently homogenous material. The experimental equation is as follows:

$$k(T) = \frac{\Delta x}{\frac{\Delta T}{\dot{Q}(T)} - 2R(T)} \tag{5}$$

where Δx is the specimen thickness, $\dot{Q}$ is the heat flow rate, ΔT is the difference in temperature between the upper and the lower plate, and $2R$ is the thermal surface resistance in the plate/specimen interface. The heat flow rate $\dot{Q}(T) = S_{\text{cal}}\Delta U(T)$ is not measured directly, but related to a calibration factor S_{cal} and the measured sensor output ΔU from the heat flux sensor.

The surface resistance is measured by using a two-thickness calibration set with a known thermal conductivity k_{cal}:

$$2R = \frac{\Delta x_2 \Delta U_2 - \Delta x_1 \Delta U_1}{k_{\text{cal}}(\Delta U_1 - \Delta U_2)} \tag{6}$$

The indices in eq. (6) indicate the calibration disk number. The thicknesses of the calibration discs must be significantly different, typically $\Delta x_2 > 2\Delta x_1$. The calibration factor is obtained in a similar fashion. There is one calibration factor for each plate, $S_{\text{cal,lower}}$ and $S_{\text{cal,upper}}$:

$$\begin{aligned} S_{\text{cal,lower}} &= \frac{\Delta T}{(\Delta x/k_{\text{cal}} + 2R)\Delta U_{\text{lower}}} \\ S_{\text{cal,upper}} &= \frac{\Delta T}{(\Delta x/k_{\text{cal}} + 2R)\Delta U_{\text{upper}}} \end{aligned} \tag{7}$$

where the subtext indicates the plate position. Note that R and S_{cal} are temperature dependent and extrapolated from calibration measurements at several temperatures.

Calibration

The instrument was calibrated at 20, 40, and 60°C using a two-thickness set of poly(methyl methacrylate) standards. Disks were 50.0 mm in diameter and 5.025 ± 0.0005 and 11.865 ± 0.0005 mm in thickness, respectively. Using a two-thickness calibration set allows for precise calculation of the surface-

Table II. Calibration Set Reference Values for the Thermal Conductivity k_{cal} at Three Mean Temperatures T

T (°C)	k_{cal} (W/(m·K))
20.00	0.1885
40.00	0.1909
60.00	0.1933

resistance correction term, increasing the accuracy of the measurement.

The thermal conductivity k_{cal} of the calibration set had been measured in a direct heat flow apparatus at National Physical Laboratory (United Kingdom) at three mean temperatures and the reported values are listed in Table II.

A minimum of 16 blocks of 256 heat flow measurements were collected for each temperature (one measurement every second), and the average values for the last six blocks were used for calculations. For each block, the specimen was required to be in the so-called perfect equilibrium, keeping the temperature stable within 0.02 K and the indirect heat flux within 40 μV. The random variation in computed thermal conductivity between the last six blocks is mostly $<1 \times 10^{-4}$ W/(m · K) with no detectable drift.

Calibration specimen and ordinary specimen surfaces were lubricated by DuPont Krytox GPL101 thermal oil. The oil was applied to reduce the thermal surface resistance of the specimens. A pipette was used to apply 5 μL to each surface, and the substance was smeared out using a glove (Latex Free Nitrile). Excess oil was wiped off with a make-up sponge.

The calibration was performed on the same week as the samples were tested and Tables III and IV list the measured surface resistances and calibration factors at the various temperatures. The calibration was checked by measuring on the 5-mm calibration disk at 20°C. The result was accepted with $\Delta k = 1 \times 10^{-4}$ W/(m · K).

Specimen Preparation

The foam specimens were taken from the same layer as the gravimetric sample and as close as possible in hoop and axial position. It was assumed that the morphology was the same as for the gravimetric sample and the slices obtained by Tofteberg et al. Eight specimens were taken from different radial positions in the foam layer at the same hoop position. Specimens were machined by a lathe into disks, nominally measuring 50 mm across and 5 mm in the thickness. The thinnest possible disks were chosen so that the morphology would change as little as possible over the thickness, effectively making a homogenous, anisotropic sample.

Table III. Surface-Resistance R Obtained from the Calibration

T (°C)	$2R$ (10^{-3} m^{2}K/W)
20.00	3.32
40.00	3.09
60.00	3.03

Table IV. Calibration Factor S_{cal} Obtained from the Calibration

T_{lower} (°C)	$S_{cal,lower}$ (W/[m$^2\mu$V])	T_{upper} (°C	$S_{cal,upper}$ (W/[m$^2\mu$V])
10.00	0.0763	30.00	0.0738
30.00	0.0755	50.00	0.0742
50.00	0.0742	70.00	0.0744

The disks were weighed in air and water (buoyancy method) at ambient temperature to obtain the mass density ρ. It was calculated that the precision in the density measurement was 2 kg/m^3. Great care was taken in selecting radial positions that would give a variety of densities and morphologies, based on the morphological data obtained previously.[21] Table V lists the radial position of the center of each disk and its mass density.

As summarized in Table V, it is evident that there is a good variation of densities, typically in steps of 6–7% between samples, and hence significant differences in the thermal conductivities should be observed. The Vicat softening temperature for the material around 90°C is well above the test temperature. Specimens were conditioned in the laboratory for 24 h prior to testing.

Thermal Conductivity Measurements

Krytox oil was applied to both surfaces of the specimen as described above for the calibration. The specimen was clamped between the plates at a sufficiently low pressure as not to cause any significant deformation. The upper plate has a swivel and link which would allow some off-parallelity and some nudging to align the surfaces in the best way. The specimens were tested at 20°C with a differential temperature $\Delta T = 20$ K. The perfect equilibrium conditions were required for a minimum of 12 blocks of data, and the thermal conductivity was calculated from the average of the next three blocks of data. The uncertainty in the measurements was <1.5%.

3D RECONSTRUCTION AND THERMAL SIMULATION

3D Reconstruction of the Foam

A 3D reconstruction of the internal structure of the foam was made by adding consecutive microtomy slices from a previous study.[21] A total sample volume of 2880 mm^3 (38 × 19 × 4

Table V. Mass Density and Radial Position of the Center of Each disk

Specimen no.	Radial position (mm)	ρ (kg/m^3)
1	−1.00	1010
3	6.00	770
4	10.00	720
6	15.00	719
7	20.00	761
8	25.00	823
9	30.00	872
10	33.50	880

The origin is the interface between the preceding layer and the foam layer. Specimen numbers 2 and 5 were never made.

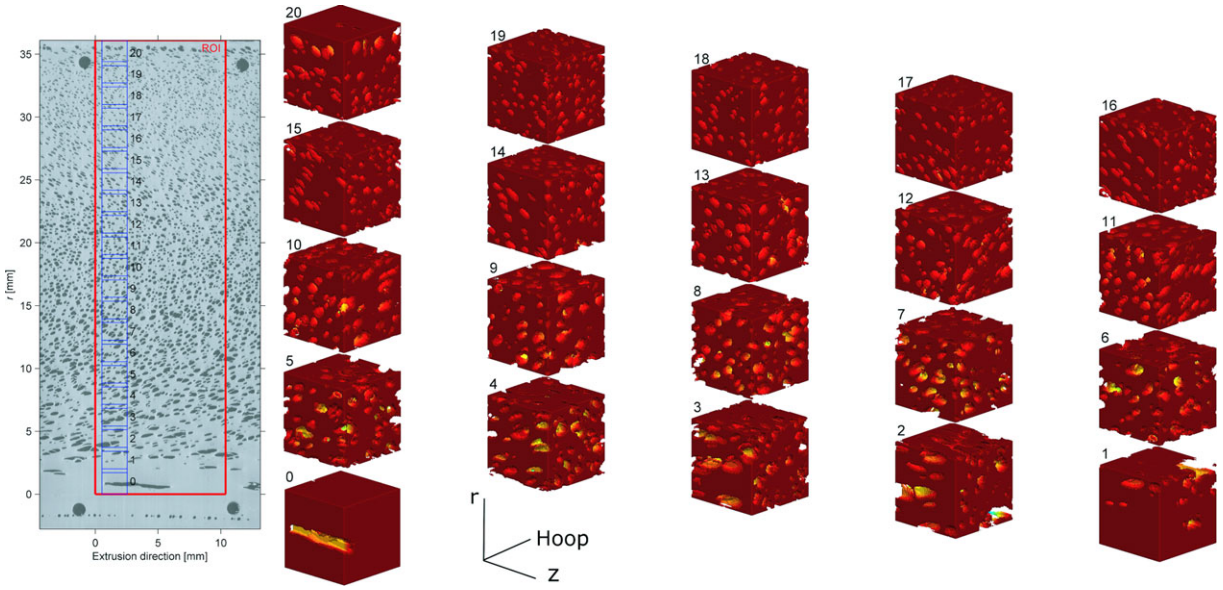

Figure 5. One of the microtome slices used for the 3D reconstruction is shown together with extracted 3D cubes. The numbers above the cubes identify the location in the slice. The face of the cube in the *rz*-plane matches the microtome slice shown. The red rectangular region of interest marks the area used to calculate the ellipse statistics shown in Figure 7. [Color figure can be viewed in the online issue, which is available at wileyonlinelibrary.com.]

mm^3) was investigated with a voxel size of 13,610 μm^3 (21.3 × 21.3 × 30 μm^3), giving a data set consisting of 212 megavoxels. To ensure correct alignment, four holes were drilled in the cuboid prior to cutting. In the image segmentation process, these holes could be clearly separated from the other bubbles by size and shape. An affine transformation of the entire image was made so that the squared distance between the locations of these four holes in a given slice and a reference slice was minimized.

Mesh from 3D Representation

From the 3D reconstruction of the internal structure of the foam, 21 cubes of 2 × 2 × 2 mm^3, rounded off to the nearest pixel, were extracted. These are shown in Figure 5. A hexagonal mesh was generated based on these cubes. Each mesh element had dimensions corresponding to one pixel in the *rz*-plane (21.2 × 21.2 μm^2) and one slice thickness in the θ-direction (30 μm). The material in the mesh element was set to solid polymer if the brightness of the relevant pixel in the relevant slice was above the global threshold value. Correspondingly, it was set to CO_2 if the brightness was below the threshold.

Thermal Simulations

Stationary thermal simulations were performed in LS-DYNA on each cube, where the governing equation was

$$0 = \vec{\nabla} \cdot (k\vec{\nabla} T) \tag{8}$$

where T is the temperature and k is the local thermal conductivity. The thermal conductivity of the matrix was set equal to that of the solid HIPS at 20°C (0.147 W/(m · K)) and the thermal conductivity of the voids was set to that of CO_2 at 1 bar and 20°C (0.015 W/(m·K)).[24] An arbitrary temperature difference of ΔT was prescribed in the radial direction. The other four sides were treated with symmetry conditions (adiabatic).The thermal conductivity of the matrix was set as a constant within the cube, that is not changing with ΔT. In reality, the thermal conductivity changes by 1.5 × 10^{-4} W/(m·K^2),[24] and an insulation system has a typical temperature gradient in the foam of 2 K/mm. The matrix thermal conductivity will therefore change by approximately 0.4% over the test cube, which is negligible.

The local thermal conductivity in the radial direction at the center location of the cube was calculated as follows:

$$k_{rr}(r) = \frac{q_r \Delta r}{A \Delta T} \tag{9}$$

where q_r is the total heat flow in *r*-direction, Δr is the height of the cube in the radial direction, and $A = \Delta z \Delta \theta$ is the area of the cube orthogonal to the *r*-axis.

RESULTS AND DISCUSSION

Foam Density

The relative density of the foam is calculated as the area fraction covered with polymer. The density extracted from image analysis is shown and compared to gravimetric measurements of the density in Figure 6. The average density from the image analysis was tuned by fitting the image segmentation grayscale threshold value, and it can be seen that the changes in density as measured using the gravimetric method are well captured using the image analysis.

There are some critical factors that might give a different density using the image analysis from a gravimetric measurement. The limited resolution of a scan can never capture the true contour of a bubble. This will lead to pixels on the border of the bubble having intermediate brightness levels. Whether these pixels are counted as bubbles or matrix will depend on how the threshold

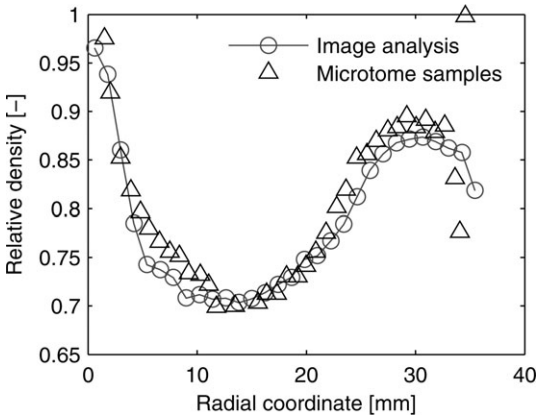

Figure 6. Calculated density using image analysis compared to gravimetric measurement of microtome slices.

value for separating foreground and background pixels is chosen. This will again influence the measured foam density.

In addition, a physical slice will always have a finite thickness, in this case 30 μm. When slicing an individual bubble, the area cross-section will then vary slightly within this thickness. When estimating the density, the correct value can be obtained if the average area occupied by the bubble within the slice thickness is used for all bubbles. However, the reason how this translates to brightness levels is not trivial.

The size, elongation, and orientation of average bubbles are shown in Figure 7. When the statistics are calculated, all bubbles are binned according to the radial coordinate of the fitted ellipse centroid as shown in Figure 7(A). The average value of the orientation, elongation, and bubble area is then calculated within each bin. All the data points shown represent an average of at least 50 ellipses.

The size of the bubbles decreases monotonically outward from the steel pipe except for a layer of large bubbles in the immediate vicinity of the outer solid polymer layer. This is shown in Figure 7(B). The mean orientation of the bubbles is shown in Figure 7(C). The most highly oriented bubbles are found at $r <$ 5 mm. Around $r = 15$ mm, the bubbles get less and less oriented. At the same time, the elongation of the bubbles [Figure 7(D)] decreases. Around $r = 20$ mm, the bubbles are nearly spherical. Moving outward in the pipe, the bubbles again become more oriented with an orientation small in absolute value and negative in sign.

Thermal Conductivity Simulations and Measurements

Thermal conductivity was simulated and measured on the innermost foam layer of the commercial pipe insulation as shown in Figure 1. In Figure 8, the simulated temperature field in cube no. 3 from Figure 5 is shown. Only the mesh elements corresponding to solid material are shown to illustrate the porosity. The isolating effect of the inclusions is seen by the curvature of the isotherms.

Apart from conduction through the matrix and voids, convection and radiation across the voids contribute to the thermal conductivity. Both contributions are neglected here. Calculations

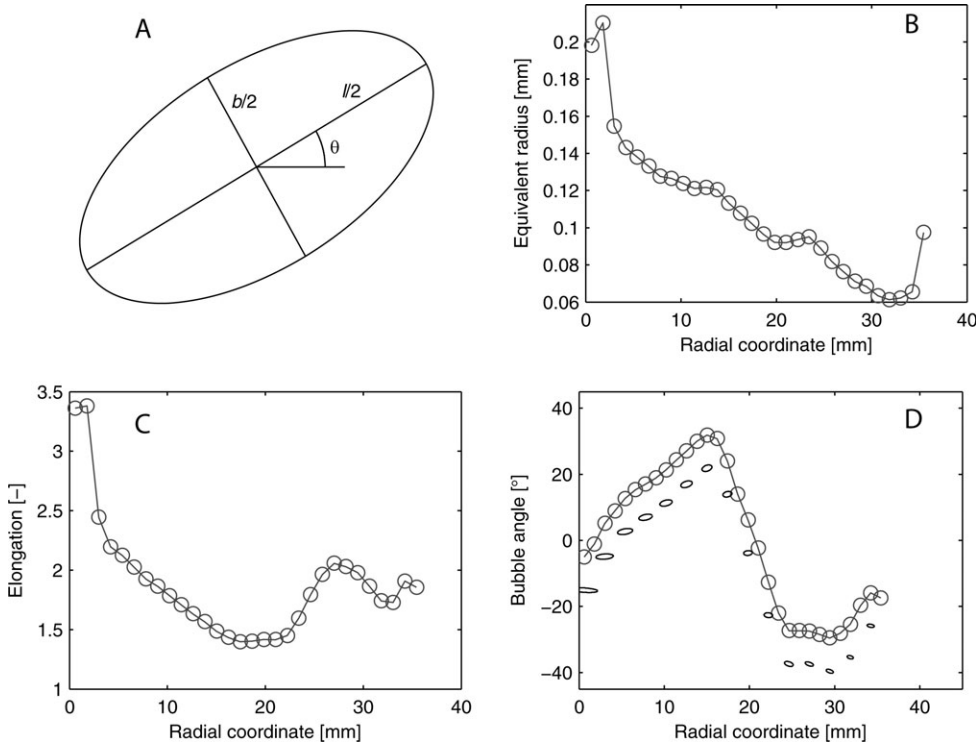

Figure 7. (A) Definition of ellipse parameters l, b, and θ. (B–D) Average ellipse parameters as a function of radial coordinate. (B) The equivalent bubble radius, $r_{eq} = \sqrt{lb/4}$. (C) The bubble elongation l/b. (D) The bubble orientation is shown together with an ellipse having the average values of l,b and θ at selected coordinates.

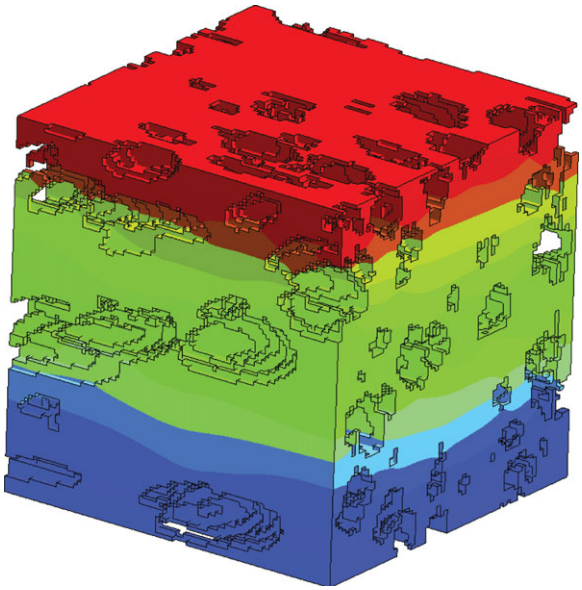

Figure 8. Simulated temperature field in one cube. The cube shown is identical to cube no. 3 in Figure 5. [Color figure can be viewed in the online issue, which is available at wileyonlinelibrary.com.]

using the Williams and Aldao model showed that the radiative contribution to the thermal conductivity of the cubes ranged from 0.2 to 0.8% for each of the cubes, and a conservative estimate based on the arguments of Harding showed that the contribution to the conductivity from convection is neglectable provided the cell size is smaller than 1 mm, which is the case here.[25–27]

For each of the cubes, the thermal conductivity in the radial direction was extracted according to eq. (9). This thermal conductivity is shown together with the relative density of the cubes in Figure 9. It is seen that the conductivity largely follows the shape of the density curve, indicating that the two are proportional. The simulated thermal conductivity deviates somewhat beyond the experimental error of the measured thermal conductivity. The error in the method needs to be investigated further, and improvements can be made in the image segmentation algorithm and by using thinner slices and a higher image resolution.

However, the measured thermal conductivities at, for instance, $r = 10.0$ mm and $r = 15.0$ mm differ by as much as 7% although the mass density is exactly the same. Similarly, relative thermal conductivity values at $r = 6.0$ mm and $r = 25.0$ mm are lower than the relative density value. Looking at the morphology in Figure 7, the difference can be explained by bubbles at 6.0, 10.0, and 25.0 mm being much more elongated, transversely to the heat flow direction than at $r = 15.0$ mm. The reduction in thermal conductivity owing to anisotropy of the bubbles is as expected; If the long axis is oriented parallel to the pipe, the heat flow out of the pipe is interrupted more than for a round bubble, or bubble oriented radially with the heat flow direction.[10,11,13] The bubbles at 25.0 mm are considerably smaller and in higher numbers, adding to the thermal resistance. It would be possible to use this method to do parametric studies of the individual morphological parameters, but the focus of this article is on describing the thermal conductivity of the whole structure.

The transverse conductivities are not presented here because the heat flow in an axisymmetric insulation layer is zero in the hoop direction, and in most cases the axial temperature gradients along the pipeline are very small and the axial heat flow can be neglected. Finding the total radial thermal conductivity $\overline{k_{rr}}$ of a foam layer is a purely 1D problem, and it can be shown that

$$\frac{1}{\overline{k_{rr}}} = \frac{1}{L}\int_{R_I}^{R_O} \frac{1}{k_{rr}(r)}\,dr \tag{10}$$

where R_O and R_I denote the outer and inner radial positions of the layer and $L = R_O - R_I$ is the foam thickness. Assuming that thermal conductivity scales linearly with density and using density measurements from the 3D geometry, $\overline{k_{rr}} = 0.113$ W/(m·K) at 20°C for this foam layer. If instead $k_{rr}(r)$ is taken from the thermal simulations in Figure 9, $\overline{k_{rr}}$ decreases by 5% to 0.107 W/(m·K). The example illustrates the importance of considering foam morphology and not only mass density.

CONCLUSIONS

A method is presented to generate the internal 3D geometry of high-density polymer foam from microtome slices and optical image analysis. The 3D geometry gives the correct density distribution within the foam. This is verified using a simple, but accurate gravimetric method. Finite element analysis is used to calculate thermal conductivity with a mesh based on the 3D geometry. The thermal simulations and measurements are in good agreement.

A typical foamed thermal insulation layer of a subsea oil and gas pipe is analyzed. The foam morphology is highly anisotropic and inhomogeneous. Results show that thermal conductivity is dependent on morphology and approximations of the thermal

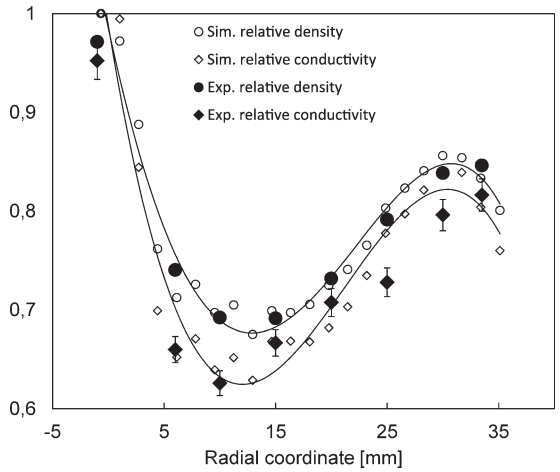

Figure 9. Simulated and experimental thermal conductivity and density as a function radial coordinate of the entire thickness of one foam layer. Both parameters are scaled relative to solid HIPS. The solid lines are polynomial fits to the simulated data set.

conductivity based on the mass density alone are not sufficiently precise. In particular, anisotropy needs to be considered. For a highly anisotropic region of the foam where the long axis of the bubble is parallel to the axial direction of the pipe, the radial thermal conductivity is 7% lower than for the less isotropic neighboring region of the foam with the same mass density.

ACKNOWLEDGMENTS

This study is part of the collaborative project "Demanding Polyolefin Applications" with the industrial partners Nexans Norway AS, Bredero Shaw Norway AS, and the research institutes Norwegian University of Science and Technology (NTNU), University of Oslo, SINTEF Materials and Chemistry, SINTEF Energy Research and Norner AS. The authors thank for the financial support by the Norwegian Research Council (grant 179945/I40), Borealis, and the industrial project partners. The authors also thank all partners in the project for constructive discussions.

REFERENCES

1. Hammerschmidt, E. G. *Ind. Eng. Chem.* **1934**, *26*, 851.
2. Hunt, A. Oil & Gas Journal; PennWell Corporation, United States, Tulsa, **1996**, *94*, p 62.
3. Mokhatab, S.; Towler, B. *World Oil* **2009**, *230*, 55.
4. Mokhatab, S.; Wilkens, R. J.; Leontaritis, K. J. *Energy Sources A* **2007**, *29*, 39.
5. Aalund, L. R. *Oil Gas J.* **1992**, *90*, 42.
6. Boye Hansen, A.; Jackson, A. 16th International Conference on Pipeline Protection, November 2–4, Paphos, Cyprus, **2005**, p 285.
7. Wilmott, M.; Highams, J.; Ross, R.; Kopystinski, A. *J. Prot. Coat. Linings* **2000**, *17*, 47.
8. Jackson, A. Proceedings of the International Conference on Offshore Mechanics and Arctic Engineering—OMAE, **2002**, *3*, 457.
9. Jackson, A.; Jackson, P.; Wan, E.; Hegdal, J. P. 18th BHR Conference on Pipeline Protection, Antwerp, Belgium, **2009**.
10. Sen, A. K.; Torquato, S. *Phys. Rev. B*, **1989**, *39*, 4504.
11. Mikdam, A.; Makradi, A.; Ahzi, S.; Garmestani, H.; Li, D. S.; Remond, Y. *Comp. Sci. Technol.* **2010**, *70*, 510.
12. Mori, T.; Tanaka, K. *Acta Metall.* **1973**, *21*, 571.
13. Leach, A. G. *J. Phys. D: Appl. Phys.* **1993**, *26*, 733.
14. Sevostianov, I.; Kachanov, M. *Int. J. Solids Struct.* **2012**, *49*, 3242.
15. Martínez-Díez, J. A.; Rodríguez-Pérez, M. A.; De Saja, J. A.; Arcos Y Rábago, L. O.; Almanza, O. A. *J. Cell. Plast.* **2001**, *37*, 21.
16. Knackstedt, M. A.; Arns, C. H.; Saadatfar, M.; Senden, T. J.; Limaye, A.; Sakellariou, A.; Sheppard, A. P.; Sok, R. M.; Schrof, W.; Steininger, H. *Proc. R Soc. Lond. A* **2006**, *462*, 2833.
17. Maire, E.; Caty, O.; Bouchet, R.; Loretz, M.; Adrien, J.. *MRS Proceedings* **2009**, p 1188.
18. Uchic, M. D.; Holzer, L.; Inkson, B. J.; Principe, E. L.; Munroe, P. *MRS Bull.* **2007**, *32*, 408.
19. Forsman, O. *Jernkontoret. Ann.* **1918**, *102*, 1.
20. Spowart, J. E. *Scripta Mater.* **2006**, *55*, 5.
21. Tofteberg, T.; Hegdal, J. P.; Larsen, A. G. Schjelderup, T.; Hinrichsen, E. L.. EUROTEC 2011 Conference, in Conjunction with EQUIPLAST, November 14–15, Barcelona, Spain, **2011**.
22. ASTM Standard C518-10, "Standard Test Method for Steady-State Thermal Transmission Properties by Means of the Heat Flow Meter Apparatus," ASTM International, West Conshohocken, PA, **2010**.
23. ISO 8301:1991(E), "Thermal Insulation—Determination of Steady-State Thermal Resistance and Related Properties—Heat Flow Meter Apparatus," International Organization for Standardization, Genève, Switzerland, **1991**.
24. TN-UL95-TC-001, "Thermotite ULTRA—Thermal Conductivity Measurement," BrederoShaw, Orkanger, Norway, **2009**.
25. Williams, R. J. J.; Aldao, C. M. *Polym. Eng. Sci.* **1983**, *23*, 293.
26. De Micco, C.; Aldao, C. M. *J. Polym. Sci. Part B: Polym. Phys.* **2005**, *43*, 190.
27. Harding, R. H. *Ind. Eng. Chem. Process Des. Dev.* **1964**, *3*, 117.